



A unified two-scale theory for modeling microstructural length scale, strain gradient and strain rate effects on brittle fracture

Yipeng Rao^{a,b}, Meizhen Xiang^{a,*}, Quanzhang Li^b, Junzhi Cui^{b,*}

^a Laboratory of Computational Physics, Institute of Applied Physics and Computational Mathematics, Beijing, 100088, China

^b LSEC, ICMSEC, Academy of Mathematics and Systems Sciences, CAS, Beijing, 100090, China

ARTICLE INFO

Keywords:

Micro-cracks
Dynamic fracture
Strain gradient
Strain rate
Microstructure effect
Two-scale method

ABSTRACT

Microstructure, strain gradient and strain rate are key factors that influence fracture of heterogeneous brittle materials. The present work for the first time unifies effects of these factors in an analytical dynamic fracture criterion based on fundamental micromechanics. By using an energy-based two-scale theory accounting for micro-inertia, we rigorously derive an formulation for microscopic dynamic energy release rate involving additive contributions of macroscopic strain, strain gradient and strain rate. The coefficients of the formulation are correlated to microstructural length scale and are calculated based on integrals of the first order microscopic cell solutions. The two-scale formulation of energy release rate, along with the Griffith law for a single micro-crack, results in a novel dynamic fracture model. The remarkable feature of this modeling approach is that, without extra phenomenological *ad hoc* hypotheses, all microstructural length scale, strain gradient and strain rate effects are natural consequences of the unified two-scale theory.

Capabilities of the dynamic fracture model for predicting coupled effects of microstructure size, strain gradient and strain rate on brittle fracture behaviors are confirmed by numerical simulations. The model is also well validated against experimental results. Especially, finite element simulations based on the model well reproduce free surface velocity profiles, fracture zones and spall strengths measured in series of dynamic spalling fracture experiments.

1. Introduction

The operative micromechanism that governs fracture in brittle materials is the nucleation, growth and coalescence of micro-cracks (Ravi-Chandar and Yang, 1997). Brittle fracture is influenced by internal factors of materials, such as microstructural characteristics and energy dissipation mechanisms at lower scales, as well as external macroscale factors, such as loading mode, strain rate and temperature. Understanding and modeling these factors and their coupling effects based on fundamental micromechanics still require greater efforts.

Firstly, understanding and predicting microstructure effects on macro mechanical behaviors have always been one of the super objectives in materials and mechanics community (Chatzigeorgiou et al., 2009; Hossain et al., 2015). For microstructure effects on fracture, the interaction mechanisms between cracks and inclusions have drawn much attention, e.g., crack trapping (Gao and Rice, 1989; Vasoya et al., 2016), crack deflection (Brach et al., 2019; Lebihain et al., 2020), crack trapping and depinning from obstacles (Chopin et al., 2018), crack denucleation/renucleation (Hossain et al., 2014; Wang and Xia, 2017) and crack bridging (Mirkhalaf et al., 2014). Recently, quantitatively

predicting macroscale fracture properties (including fracture toughness, fracture strength and fracture surface roughness) as a function of microstructure becomes one of the most prolific topics in fracture mechanics. For example, Liu and Gao (2021) confirmed Hall-Petch relation in the fracture strength of matrix-body crystalline diamond compact bit. Ramanathan et al. (1997) studied the dynamics of a single crack moving through a heterogeneous medium and found that the crack surface is self-affine with a roughness exponent of 0.5 for tearing loading while a crack surface is only logarithmically rough under tensile loading. Li and Zhou (2013a,b) developed a cohesive finite element method based multi-scale framework for analyzing the effects of microstructural heterogeneity, phase morphology, phase size, constituent behavior, and interfacial bonding strength on the fracture toughness of materials. The computational framework allows the fracture initiation toughness and propagation toughness to be predicted as functions of microstructural attributions and constituent behavior. Similar computational strategy is adopted by Roy and Zhou (2020) to explore the fracture processes in microstructured metals and relate their fracture toughness to microstructure attributes such as grain boundary strength

* Corresponding authors.

E-mail addresses: xiang.meizhen@iapcm.ac.cn (M. Xiang), cjz@lsec.cc.ac.cn (J. Cui).

<https://doi.org/10.1016/j.ijsolstr.2023.112176>

Received 28 October 2022; Received in revised form 4 February 2023; Accepted 19 February 2023

Available online 21 February 2023

0020-7683/© 2023 Elsevier Ltd. All rights reserved.

distribution, grain size, and constituent plasticity level. Lebihain et al. (2021) carried out numerical and theoretical investigation on the strong impact of microstructural features on macro crack propagation and the fracture resistance of three-dimensional disordered brittle solids. Other investigations concerns the propagation of micro-cracks and its connection with macro mechanical state. Rafiee et al. (2004) carried out numerical investigation on micro-crack nucleation in front of a fast running macro-crack and shown increasing fracture toughness and energy dissipation with increasing crack speed. Dascalu et al. (2008) and Keita et al. (2014) derived microstructure-related energy release rate and fracture model accounting for micro-crack nucleation and growth, which reproduces experimentally known behaviors, like the localization of damage and size-dependence of the structural response.

When the largest microstructural scale in a material approaches the relevant macroscopic structure scale, classical continuum mechanics, which fundamentally assumes local dependence between stress and strain, fails to capture the significant scale effects related to microscale nonlocal interactions (Peerlings and Fleck, 2004; Smyshlyayev and Cherednichenko, 2000; Li, 2011; Li et al., 2011). Driven by the needs to describe scale effects, generalized nonlocal continuum mechanics are promoted. One way to generalize continuum mechanics is to involve strain gradient term in constitutive equations. Strain gradient theory for elasticity has been studied since 1960s (Toupin, 1962, 1964; Mindlin, 1965; Mindlin and Eshel, 1968; Lam et al., 2003; Lazopoulos, 2004). The strain gradient theory has a period of vigorous development since 1990s when it is applied to the theory of plasticity (Fleck and Hutchinson, 1993; Hutchinson and Fleck, 1997; Gao et al., 1999; Fleck and Hutchinson, 2001; Huang et al., 2000; Lazar et al., 2006). In damage and fracture mechanics, strain gradient theories are used to regular the classical singularity stress and strain fields around crack tip (Chen et al., 1999; Jiang et al., 2001; Po et al., 2014; Makvandi et al., 2019; Vasiliev et al., 2021). In addition, strain gradient is also incorporated into fracture criterion or damage evolution equations in materials with many micro-cracks inside (Peerlings et al., 1996; Li, 2011; Li et al., 2011; Kuliev and Morozov, 2016; Nguyen and Niiranen, 2020; Rao et al., 2022).

Under dynamic loading, strain rate is a crucial factor that influences fracture behaviors. For a variety of materials, crack growth resistance is found to increase with increasing loading rate (Ozbolt et al., 2014; Rittel and Maigre, 1996; Owen et al., 1998). Size distribution of fragments (Grady, 1988) and fracture surface roughness (Osovski et al., 2015) are also influenced by strain rate. Moreover, transition of fracture modes may occur under high strain rates. Brittle-to-ductile transition (Gilath et al., 1988) or ductile-to-brittle transition (Li et al., 2016) may occur depending on loading conditions and material category. A typical dynamic fracture mode widely probed in laboratories is shock-induced spalling fracture, which occurs when rarefaction waves resulted from reflection of compression shock waves at stress-free surfaces interacts to form tensile stresses (Antoun et al., 2003). Impact loading may lead to spalling fracture at strain rates about $10^4 - 10^6 \text{ s}^{-1}$ (Xiang et al., 2021) while laser loading may leads to spalling fracture at strain rates of $10^6 - 10^9 \text{ s}^{-1}$ (Jarmakani et al., 2010). Spalling experiments have become a standard way to probe dynamic material properties under extremely high strain rates. The fracture strength measured in spalling experiments are referred to as spall strength whose rate-dependence has been widely investigated (Erzar and Buzaud, 2012; Zinszner et al., 2015).

The main contribution of the present work is a rigorous two-scale theory that unifies microstructural length scale, strain gradient and strain rate effects on fracture. It is established by adding micro-inertia effects into the energy-based two-scale asymptotic theory proposed in a former work by the authors (Rao et al., 2022). Based on the two-scale theory, we rigorously derive an analytical formulation for microscopic dynamic energy release rate, which, along with the Griffith law for single micro-crack, results in a novel dynamic fracture model. The notable feature of this modeling approach is that microstructural

length scale, strain gradient and strain rate effects on fracture are all natural consequences of the two-scale energy analysis procedure without extra *ad hoc* hypotheses. The resulted formulation for microscopic dynamic energy release rate involves additive contributions of macroscopic strain, strain gradient and strain rate. The coefficients of the formulation are correlated to microstructural size and the first order cell solutions. Prediction capabilities of the resulted novel dynamic fracture model are confirmed by numerical simulations on macro material point responses, crack propagation in a V-notch plate and spalling fracture, in comparison with available experimental data.

We note that a recently developed multiscale method called Method of Multiscale Virtual Power (MMVP) have also accounted for micro-inertia and strain gradient effects (De Souza Neto et al., 2015; Blanco et al., 2016a,b; Rocha et al., 2021). The MMVP theory lies on the generalized Hill–Mandel Principle of Macrohomogeneity, along with definitions of two-scale kinematical admissibility and duality. The MMVP method is powerful allowing for treatment of problems involving phenomena as diverse as dynamics, higher order strain effects, material failure with kinematical discontinuities, fluid mechanics and coupled multi-physics. However, the present work is quite different from the MMVP approach. Firstly, the two-scale analysis procedure of the present work lies on the math-based two-scale asymptotic theory, instead of the generalized Hill–Mandel Principle of Macrohomogeneity. In the present approach, the microscale displacement and velocity fields are accurately determined by partial differential equations derived from the two-scale asymptotic theory, with no prior kinematical assumptions required. Secondly, the present modeling approach results in a novel analytical dynamic fracture criterion that explicitly involves microstructural length scale, macro strain, strain gradient and strain rate. Such results have not been reported in works related to MMVP.

The paper is organized as follows. In Section 2, a two-scale analysis framework involving micro-inertia effects for brittle materials with amount of micro-cracks inside is established. In Section 3, the model for micro-crack propagation and macro fracture is derived through energy analysis based on the two-scale asymptotic theory. Numerical results and comparisons with experiments are shown in Section 4. And the work is concluded in Section 5. Throughout this paper, the Einstein summation convention for repeated indices is adopted.

2. Modeling

2.1. Macro problem

We consider a macroscopic bounded elastic solid Ω in the two-dimensional space. Amount of micro-cracks, which are not explicitly visible at the macroscale, randomly distributes in the solid. In the two-scale modeling approach, mechanical responses of a macroscale material point is described by a representative volume element (RVE) containing micro-cracks. Especially, macro fracture is attributed to extension and coalescence of micro-cracks. We assume that all the micro-cracks are periodically aligned in the RVE following a preferential direction and that they extend in mode slowromancapi@, as illustrated in Fig. 1. Such simplifications on micro-crack distribution reduce the model complexity. They are suitable for some typical fracture phenomena, like spalling (Antoun et al., 2003), where micro-cracks preferentially develop in one direction and in mode slowromancapi@. We also anticipate here that limitation of such simplifications is obvious. For example, it cannot capture micro-cracking with rotating propagation direction and micro-cracking with mixed mode. In the RVE, the average distance between two adjacent micro-cracks is denoted by ϵ , which is also the length the periodical cell. A cell with side length ϵ containing a linear micro-crack is denoted by Y_ϵ , the length of the micro-crack is denoted by l , and the normalized micro-crack length is defined as $d = l/\epsilon$ which measures local damage state of a macro material point. $d = 1$ means coalescence of micro-cracks and indicates complete rupture of the macro material point. A microscale

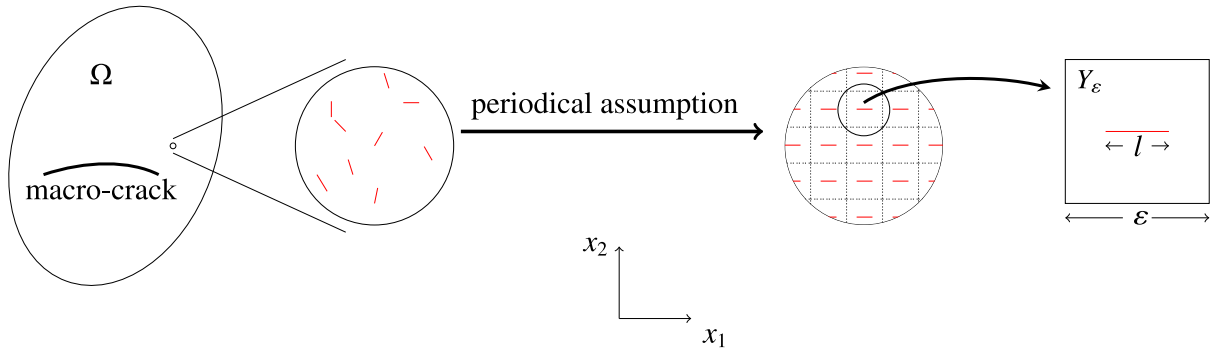


Fig. 1. Illustration of the two scale modeling framework and the local periodic assumption.

coordinate system (x_1, x_2) is defined for the RVE with x_1 being along the micro-crack and x_2 perpendicular to the micro-crack.

The macroscopic momentum equation can be written as

$$\frac{\partial \Sigma_{ij}}{\partial X_j} = \rho \frac{\partial^2 U_i}{\partial t^2} \quad \text{in } \Omega \quad (1)$$

where ρ is the density of the solid, U is the displacement field, $\{\Sigma_{ij}\}$ is macro stress tensor and X is coordinates in the macro structure. Before failure, the macro stress-strain relation is

$$\Sigma_{ij} = C_{ijkl} \mathcal{E}_{kl} \quad (2)$$

where $\{C_{ijkl}\}$ is the homogenized elastic tensor which depends on microstructure and \mathcal{E} is macro strain tensor:

$$\mathcal{E}_{ij} = \frac{1}{2} \left(\frac{\partial U_i}{\partial X_j} + \frac{\partial U_j}{\partial X_i} \right). \quad (3)$$

Based on the two-scale asymptotic theory, the homogenized elastic tensor $\{C_{ijkl}\}$ is only dependent on d and is independent of ε . The detailed expression of $\{C_{ijkl}\}$ is presented in Section 2.2 of this work and can also be found in Rao et al. (2022).

2.2. Two-scale asymptotic analysis

We denote the infinite periodical RVE as $B(= \mathbb{R}^2)$ and the domain occupied by micro-cracks as C . The solid part in the RVE is $B_s = B \setminus C$. The momentum equilibrium equation in the RVE is

$$\frac{\partial \sigma_{ij}^\varepsilon}{\partial x_j} = \rho \frac{\partial^2 u_i^\varepsilon}{\partial t^2}, \quad \text{in } B_s. \quad (4)$$

The linear elastic constitutive relation is adopted:

$$\sigma_{ij}^\varepsilon = a_{ijkl} e_{kl}(\mathbf{u}^\varepsilon) \quad (5)$$

where \mathbf{u}^ε , σ^ε and $e_{ij}(\mathbf{u}^\varepsilon)$ represent displacement, stress and strain fields respectively,

$$e_{ij}(\mathbf{u}^\varepsilon) = \frac{1}{2} \left(\frac{\partial u_i^\varepsilon}{\partial x_j} + \frac{\partial u_j^\varepsilon}{\partial x_i} \right). \quad (6)$$

We assume isotropic elasticity of the solid in the RVE:

$$a_{ijkl} = \lambda \delta_{ij} \delta_{kl} + \mu (\delta_{ik} \delta_{jl} + \delta_{il} \delta_{jk}) \quad (7)$$

where λ and μ are the Lamé constants and δ_{ij} is the Kronecker symbol.

We only consider micro-crack extension and ignore micro-crack closure. Thus, the following unstressed boundary condition at crack surfaces is adopted,

$$\sigma^\varepsilon \cdot \mathbf{n} = 0, \quad \text{on } C^+ \text{ and } C^- \quad (8)$$

where C^+ and C^- represent the crack surfaces and \mathbf{n} is the outward unit normal vector on crack surfaces.

Using scale-transformation $\mathbf{y} = \mathbf{x}/\varepsilon$, the periodicity cell Y_ε is mapped to a unit reference cell $Y = [0, 1] \times [0, 1]$ (see Fig. 2). Correspondingly,

the crack C maps to C_Y with length $d = l/\varepsilon$ in Y . The crack surfaces in the unit reference cell is denoted as C_Y^+ , C_Y^- and the solid part in the reference cell is denoted as $Y_s = Y \setminus C_Y$. The two distinct scales are represented by the variables \mathbf{x} , which are referred to as *slow* or *macroscopic* variables and the variables $\mathbf{y} = \mathbf{x}/\varepsilon$, referred to as *fast* or *microscopic* variables (Dascalu et al., 2008). Let $\Psi = \Psi(\mathbf{x}, \mathbf{y})$ be an arbitrary function depends on the slow and fast variables. It can be rewritten as a function Ψ_ε which depends only on one variable \mathbf{x} , i.e.,

$$\Psi_\varepsilon(\mathbf{x}) = \Psi(\mathbf{x}, \mathbf{x}/\varepsilon) \quad (9)$$

Defining $\frac{d\Psi}{d\mathbf{x}} = \frac{d\Psi_\varepsilon}{d\mathbf{x}}$ implies the following chain rule of spatial derivatives:

$$\frac{d\Psi}{d\mathbf{x}} = \frac{\partial \Psi}{\partial \mathbf{x}} + \frac{1}{\varepsilon} \frac{\partial \Psi}{\partial \mathbf{y}}. \quad (10)$$

To simplify the formulations in following derivations, we introduce notation e_{xij} and e_{yij} for symmetric parts of spatial derivatives of a vector function $\Psi(\mathbf{x}, \mathbf{y})$, i.e.,

$$e_{xij}(\Psi) = \frac{1}{2} \left(\frac{\partial \Psi_i}{\partial x_j} + \frac{\partial \Psi_j}{\partial x_i} \right), \quad e_{yij}(\Psi) = \frac{1}{2} \left(\frac{\partial \Psi_i}{\partial y_j} + \frac{\partial \Psi_j}{\partial y_i} \right).$$

According to the asymptotic homogenization method (Cioranescu and Donato, 1999), the RVE solution \mathbf{u}^ε is formally expressed as

$$\mathbf{u}^\varepsilon(\mathbf{x}, t) = \mathbf{u}^{(0)}(\mathbf{x}, \mathbf{y}, t) + \varepsilon \mathbf{u}^{(1)}(\mathbf{x}, \mathbf{y}, t) + \varepsilon^2 \mathbf{u}^{(2)}(\mathbf{x}, \mathbf{y}, t) + \dots \quad (11)$$

where $\mathbf{u}^{(i)}(\mathbf{x}, \mathbf{y}, t)$, $(i \in \mathbb{N})$ are Y -periodic about micro variable \mathbf{y} . By substituting the asymptotic expansion (11) into (4) and gathering the terms for each order of ε , we obtain the following partial differential equations defined in the unit cell:

$$\begin{cases} \frac{\partial}{\partial y_j} (a_{ijkl} e_{ykl}(\mathbf{u}^{(0)})) = 0, & \text{in } Y_s, \\ a_{ijkl} e_{ykl}(\mathbf{u}^{(0)}) n_j = 0, & \text{on } C_Y^\pm; \end{cases} \quad (12)$$

$$\begin{cases} \frac{\partial}{\partial y_j} (a_{ijkl} (e_{xkl}(\mathbf{u}^{(0)}) + e_{ykl}(\mathbf{u}^{(1)}))) = 0, & \text{in } Y_s, \\ a_{ijkl} (e_{xkl}(\mathbf{u}^{(1)}) + e_{ykl}(\mathbf{u}^{(0)})) n_j = 0, & \text{on } C_Y^\pm; \end{cases} \quad (13)$$

$$\begin{cases} \frac{\partial}{\partial x_j} a_{ijkl} (e_{xkl}(\mathbf{u}^{(0)}) + e_{ykl}(\mathbf{u}^{(1)})) \\ + \frac{\partial}{\partial y_j} a_{ijkl} (e_{xkl}(\mathbf{u}^{(1)}) + e_{ykl}(\mathbf{u}^{(2)})) = \rho \frac{\partial^2 u_i^{(0)}}{\partial t^2}, & \text{in } Y_s, \\ a_{ijkl} (e_{xkl}(\mathbf{u}^{(1)}) + e_{ykl}(\mathbf{u}^{(2)})) n_j = 0, & \text{on } C_Y^\pm. \end{cases} \quad (14)$$

where

$$D(Y_s) = \left\{ \mathbf{u} \mid \mathbf{u} \in [H^1(Y_s)]^2, \mathbf{u} \text{ is } Y\text{-periodic in } \mathbf{y}, \int_{Y_s} \mathbf{u} \, d\mathbf{y} = 0 \right\}.$$

with $H^1(Y_s)$ being the Sobolev space (Cioranescu and Donato, 1999).

According to (12), $\mathbf{u}^{(0)}$ is independent of the microscopic variable \mathbf{y} , i.e., $\mathbf{u}^{(0)} = \mathbf{u}^{(0)}(\mathbf{x})$ (Cioranescu and Donato, 1999). In the two-scale

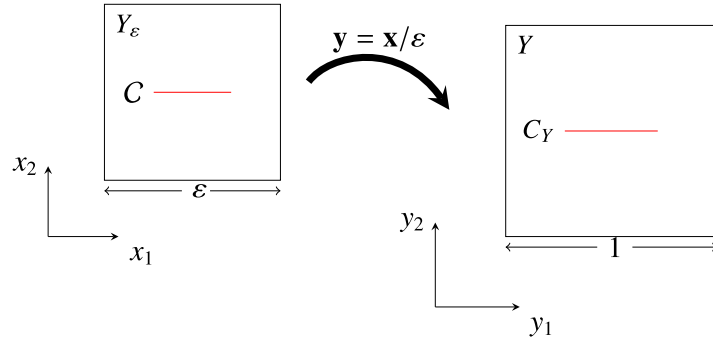


Fig. 2. Scale transformation.

asymptotic expansion theory, $\mathbf{u}^{(1)}$ is expressed in the variable separation form as

$$\mathbf{u}^{(1)}(\mathbf{x}, \mathbf{y}, t) = \mathbf{N}^{pq}(\mathbf{y}) e_{xpq}(\mathbf{u}^{(0)}(\mathbf{x}, t)) \quad (15)$$

where $\mathbf{N}^{pq}(\mathbf{y}) \in \mathcal{D}(Y_s)$, $(p, q = 1, 2)$ are the first-order cell solutions satisfying

$$\begin{cases} \frac{\partial}{\partial y_j} (a_{ijkl} e_{ykl}(\mathbf{N}^{pq}) + a_{ijpq}) = 0, & \text{in } Y_s, \\ (a_{ijkl} e_{ykl}(\mathbf{N}^{pq}) + a_{ijpq}) n_j = 0, & \text{on } C_Y^\pm. \end{cases} \quad (16)$$

It is obvious that $\mathbf{N}^{pq}(\mathbf{y}) = \mathbf{N}^{qp}(\mathbf{y})$ due to the symmetry of a_{ijkl} .

Integrating (14) over Y_s , we obtain

$$\frac{\partial}{\partial x_j} \int_{Y_s} a_{ijkl} (e_{xkl}(\mathbf{u}^{(0)}) + e_{ykl}(\mathbf{u}^{(1)})) d\mathbf{y} = \int_{Y_s} \rho \frac{\partial^2 u_i^{(0)}}{\partial t^2} d\mathbf{y}. \quad (17)$$

By substituting (15) into (17), we obtain:

$$\frac{\partial}{\partial x_j} (C_{ijkl} e_{xkl}(\mathbf{u}^{(0)})) = \rho \frac{\partial^2 u_i^{(0)}}{\partial t^2}, \quad (18)$$

where

$$C_{ijkl} = \int_{Y_s} a_{ijkl} + a_{ijmn} e_{ymn}(\mathbf{N}^{kl}) d\mathbf{y}. \quad (19)$$

Eq. (18) is the homogenization equation, which is independent of microscopic variables and parameters. From (19), we find that each component C_{ijkl} depends on Y_s through integral region and first-order cell solution \mathbf{N}^{kl} . Therefore, C_{ijkl} depends on the damage variable d and it is independent of microstructure parameter ϵ .

3. Dynamic fracture model based on two-scale asymptotic analysis

In this section, we conduct energy analysis and derive the dynamic fracture model. We assume that micro-crack extends straightly along the original direction with a same rate on both sides. We use $\langle \cdot \rangle$ to represent volume average over Y_ϵ , i.e.,

$$\langle \cdot \rangle = \frac{1}{|Y_\epsilon|} \int_{Y_\epsilon} \cdot d\mathbf{x}.$$

The volume averages of strain, strain gradients, and strain rate over Y_ϵ relate to the macroscale counterparts and consequently do not depend on the microstructural parameter d .

The strain energy W in a cell is (Rao et al., 2022):

$$W = \frac{\epsilon^2}{2} C_{pqkl} \langle e_{xpq}(\mathbf{u}^{(0)}) \rangle \langle e_{xkl}(\mathbf{u}^{(0)}) \rangle + \frac{\epsilon^4}{2} D_{pqjmn} \left\langle \frac{\partial e_{xpq}(\mathbf{u}^{(0)})}{\partial x_j} \right\rangle \left\langle \frac{\partial e_{xmn}(\mathbf{u}^{(0)})}{\partial x_l} \right\rangle \quad (20)$$

where \mathbf{D} is a sixth-order tensor with components

$$D_{pqjmn} = \int_{Y_s} a_{ijkl} \mathbf{N}_i^{pq}(\mathbf{y}) \mathbf{N}_k^{mn}(\mathbf{y}) d\mathbf{y}. \quad (21)$$

Similar to C_{ijhk} , D_{pqjmn} is also dependent on the damage variable d and is independent of ϵ . The symmetry of a_{ijkl} and the first-order cell solutions \mathbf{N}^{pq} lead to the symmetry $D_{pqjmn} = D_{qpjmn} = D_{mnlpq}$.

The local kinetic energy density in the cell is $T = \frac{1}{2} \rho \frac{\partial \mathbf{u}^\epsilon}{\partial t} \frac{\partial \mathbf{u}^\epsilon}{\partial t}$. The total kinetic energy of a cell K can be written as

$$K = \int_{Y_\epsilon} T d\mathbf{x} = \int_{Y_\epsilon} \frac{1}{2} \rho \frac{\partial \mathbf{u}^\epsilon}{\partial t} \frac{\partial \mathbf{u}^\epsilon}{\partial t} d\mathbf{x}. \quad (22)$$

We take the following first order $O(\epsilon)$ approximation in (11):

$$\mathbf{u}^\epsilon(\mathbf{x}, t) = \mathbf{u}^0(\mathbf{x}, t) + \epsilon \mathbf{u}^1(\mathbf{x}, \mathbf{y}, t) = \mathbf{u}^0(\mathbf{x}, t) + \epsilon \mathbf{N}^{pq}(\mathbf{y}) e_{xpq}(\mathbf{u}^{(0)}(\mathbf{x}, t)). \quad (23)$$

Noting that \mathbf{u}^0 and its derivatives are slowly varying functions over the local domain Y_ϵ , we rewrite K by substituting (23) into (22) to obtain

$$\begin{aligned} K &= \int_{Y_\epsilon} \frac{1}{2} \rho \frac{\partial \left(\mathbf{u}^0(\mathbf{x}, t) + \epsilon \mathbf{N}^{pq} \left(\frac{\mathbf{x}}{\epsilon} \right) e_{xpq}(\mathbf{u}^{(0)}(\mathbf{x}, t)) \right)}{\partial t} \cdot \frac{\partial \left(\mathbf{u}^0(\mathbf{x}, t) + \epsilon \mathbf{N}^{mn} \left(\frac{\mathbf{x}}{\epsilon} \right) e_{xmn}(\mathbf{u}^{(0)}(\mathbf{x}, t)) \right)}{\partial t} d\mathbf{x} \\ &= \int_{Y_\epsilon} \frac{1}{2} \rho \frac{\partial \mathbf{u}^0}{\partial t} \frac{\partial \mathbf{u}^0}{\partial t} d\mathbf{x} + \int_{Y_\epsilon} \epsilon \rho \frac{\partial \mathbf{u}^0}{\partial t} \cdot \frac{\partial \left(\mathbf{N}^{pq} \left(\frac{\mathbf{x}}{\epsilon} \right) e_{xpq}(\mathbf{u}^{(0)}(\mathbf{x}, t)) \right)}{\partial t} d\mathbf{x} \\ &\quad + \int_{Y_\epsilon} \frac{\epsilon^2}{2} \rho \frac{\partial \left(\mathbf{N}^{pq} \left(\frac{\mathbf{x}}{\epsilon} \right) e_{xpq}(\mathbf{u}^{(0)}(\mathbf{x}, t)) \right)}{\partial t} \cdot \frac{\partial \left(\mathbf{N}^{mn} \left(\frac{\mathbf{x}}{\epsilon} \right) e_{xmn}(\mathbf{u}^{(0)}(\mathbf{x}, t)) \right)}{\partial t} d\mathbf{x} \\ &\approx \frac{\epsilon^2}{2} \rho \left\langle \frac{\partial u_i^0}{\partial t} \right\rangle \left\langle \frac{\partial u_i^0}{\partial t} \right\rangle + \epsilon \rho \left\langle \frac{\partial e_{xpq}(\mathbf{u}^{(0)}(\mathbf{x}, t))}{\partial t} \right\rangle \left\langle \frac{\partial u_i^0}{\partial t} \right\rangle \\ &\quad \times \int_{Y_\epsilon} \mathbf{N}_i^{pq} \left(\frac{\mathbf{x}}{\epsilon} \right) d\mathbf{x} \\ &\quad + \frac{\epsilon^2}{2} \rho \left\langle \frac{\partial e_{xpq}(\mathbf{u}^{(0)}(\mathbf{x}, t))}{\partial t} \right\rangle \left\langle \frac{\partial e_{xmn}(\mathbf{u}^{(0)}(\mathbf{x}, t))}{\partial t} \right\rangle \\ &\quad \times \int_{Y_\epsilon} \mathbf{N}_i^{pq} \left(\frac{\mathbf{x}}{\epsilon} \right) \mathbf{N}_i^{mn} \left(\frac{\mathbf{x}}{\epsilon} \right) d\mathbf{x} \\ &\stackrel{y=\mathbf{x}/\epsilon}{=} \frac{\epsilon^2}{2} \rho \left\langle \frac{\partial u_i^0}{\partial t} \right\rangle \left\langle \frac{\partial u_i^0}{\partial t} \right\rangle + \frac{\epsilon^4}{2} \rho \left\langle \frac{\partial e_{xpq}(\mathbf{u}^{(0)}(\mathbf{x}, t))}{\partial t} \right\rangle \\ &\quad \times \left\langle \frac{\partial e_{xmn}(\mathbf{u}^{(0)}(\mathbf{x}, t))}{\partial t} \right\rangle \int_{Y_s} \mathbf{N}_i^{pq}(\mathbf{y}) \mathbf{N}_i^{mn}(\mathbf{y}) d\mathbf{y} \\ &= \frac{\epsilon^2}{2} \rho \left\langle \frac{\partial u_i^0}{\partial t} \right\rangle \left\langle \frac{\partial u_i^0}{\partial t} \right\rangle + F_{pqmn} \frac{\epsilon^4}{2} \rho \left\langle \frac{\partial e_{xpq}(\mathbf{u}^{(0)}(\mathbf{x}, t))}{\partial t} \right\rangle \\ &\quad \times \left\langle \frac{\partial e_{xmn}(\mathbf{u}^{(0)}(\mathbf{x}, t))}{\partial t} \right\rangle, \end{aligned} \quad (24)$$

where

$$F_{pqmn} = \int_{Y_s} \mathbf{N}_i^{pq}(\mathbf{y}) \mathbf{N}_i^{mn}(\mathbf{y}) d\mathbf{y}. \quad (25)$$

From (25), each component of the fourth order tensor \mathbf{F} is a function of the damage variable d and is independent of ϵ , similar to \mathbf{C} and \mathbf{D} . Based on the symmetry of the first-order cell solutions (see details in Rao et al. (2022)), we obtain $F_{pqmn} = F_{qpmn} = F_{mnpq}$ and confirm that there are only four non-zero independent components of \mathbf{F} :

$$F_{1111}, F_{1212}, F_{2222}, F_{1122}.$$

In deriving (24), the term corresponding to ϵ^3 is nil due to $\int_{Y_s} \mathbf{N}_i^{pq}(\mathbf{y}) d\mathbf{y} = 0$ for $\mathbf{N}_i^{pq}(\mathbf{y}) \in D(Y_s)$. From (24), the kinetic energy K is divided into two terms: the first term is calculated by homogenized velocity; the second term is the contribution of the fluctuations of micro-scale inertia about the volume averages to total kinetic energy.

The variation of mechanical energy with respect to the increment of the normalized micro-crack length is

$$\begin{aligned} \delta(W + K) = & \frac{\epsilon}{2} C'_{ijkl}(d) \delta d \langle e_{xij}(\mathbf{u}^0) \rangle \langle e_{xkl}(\mathbf{u}^0) \rangle + \frac{\epsilon^3}{2} D'_{pqjmn}(d) \delta d \\ & \times \left\langle \frac{\partial e_{xpq}(\mathbf{u}^0)}{\partial x_j} \right\rangle \left\langle \frac{\partial e_{xmn}(\mathbf{u}^0)}{\partial x_l} \right\rangle \\ & + \frac{\epsilon^3}{2} \rho F'_{pqmn}(d) \delta d \left\langle \frac{\partial e_{xpq}(\mathbf{u}^0)}{\partial t} \right\rangle \left\langle \frac{\partial e_{xmn}(\mathbf{u}^0)}{\partial t} \right\rangle, \end{aligned} \quad (26)$$

which represents the dissipated energy due to the propagation of micro-crack. Here, the superscript ' represents derivatives, i.e., $C'_{ijkl}(d) = \frac{dC_{ijkl}(d)}{dd}$, $D'_{pqjmn}(d) = \frac{dD_{pqjmn}(d)}{dd}$ and $F'_{pqmn}(d) = \frac{dF_{pqmn}(d)}{dd}$. The dynamic energy release rate of a micro-crack in the RVE cell is obtained as (Lemaitre and Chaboche, 1994)

$$G^{\text{dy}} = -\frac{d(W + K)}{dl} = -\frac{1}{\epsilon} \frac{d(W + K)}{dd}. \quad (27)$$

From Eqs. (20), (24), (26) and (27), we obtain

$$\begin{aligned} G^{\text{dy}} = & -\frac{\epsilon}{2} C'_{ijkl}(d) \langle e_{xij}(\mathbf{u}^0) \rangle \langle e_{xkl}(\mathbf{u}^0) \rangle - \frac{\epsilon^3}{2} D'_{pqjmn}(d) \\ & \times \left\langle \frac{\partial e_{xpq}(\mathbf{u}^0)}{\partial x_j} \right\rangle \left\langle \frac{\partial e_{xmn}(\mathbf{u}^0)}{\partial x_l} \right\rangle \\ & - \frac{\epsilon^3}{2} \rho F'_{pqmn}(d) \left\langle \frac{\partial e_{xpq}(\mathbf{u}^0)}{\partial t} \right\rangle \left\langle \frac{\partial e_{xmn}(\mathbf{u}^0)}{\partial t} \right\rangle. \end{aligned} \quad (28)$$

By comparing (24) and (28), we find that only the fluctuations of micro-scale inertia about the volume averages contributes to the dynamic energy release rate. The macro kinetic energy (the first term in the right hand side of (24)) would not affect the fracture behavior. Similar results, namely the fluctuations of micro-scale inertia about their RVE volume averages may affect the micro-scale equilibrium problem and the resulting homogenized stress, have been reported based on the MMVP approach (De Souza Neto et al., 2015; Blanco et al., 2016a,b).

The volume average of strain, strain gradients and strain rate over a periodic cell can be viewed as macroscopic counterparts, i.e.,

$$\mathcal{E}_{ij} = \langle e_{xij}(\mathbf{u}^0) \rangle, \quad \mathcal{E}_{ij,k} = \left\langle \frac{\partial e_{xij}(\mathbf{u}^0)}{\partial x_k} \right\rangle, \quad \dot{\mathcal{E}}_{ij} = \left\langle \frac{\partial e_{xij}(\mathbf{u}^0)}{\partial t} \right\rangle. \quad (29)$$

Therefore, the dynamic energy release rate for micro-crack propagation is rewritten as

$$G^{\text{dy}} = -\frac{\epsilon}{2} C'_{ijkl}(d) \mathcal{E}_{ij} \mathcal{E}_{kl} - \frac{\epsilon^3}{2} D'_{pqjmn}(d) \mathcal{E}_{pq,j} \mathcal{E}_{mn,l} - \frac{\epsilon^3}{2} \rho F'_{pqmn}(d) \dot{\mathcal{E}}_{pq} \dot{\mathcal{E}}_{mn}. \quad (30)$$

Now we introduce the Griffith law dynamic propagation of a micro-crack depends on critical energy release rate G_c , which is generally a function of crack propagation rate v , i.e., $G_c = G_c(v)$ (Gross and Seelig,

2017). The specific function form of $G_c(v)$ may be material-dependent. The crack propagation rate is related to \dot{d} as $v = \frac{\dot{d}}{2} = \frac{\epsilon \dot{d}}{2}$. Thus, we obtain the following equation for describing dynamic growth of micro-cracks by combining the Griffith law and the dynamic energy release rate:

$$\begin{aligned} & -\frac{\epsilon}{2} C'_{ijhk}(d) \mathcal{E}_{ij} \mathcal{E}_{kl} - \frac{\epsilon^3}{2} D'_{pgjmn}(d) \mathcal{E}_{pq,j} \mathcal{E}_{mn,l} \\ & - \frac{\epsilon^3}{2} \rho F'_{pqmn}(d) \dot{\mathcal{E}}_{pq} \dot{\mathcal{E}}_{mn} = G_c \left(\frac{\epsilon \dot{d}}{2} \right). \end{aligned} \quad (31)$$

This is a two-scale model where growth of micro-crack (represented by d and \dot{d}) is related to macro mechanical state variables (strain, strain gradient, and strain rate) as well as the microstructural size (average micro-crack separation) ϵ . Fracture of a macro material point occurs when the micro-cracks fully penetrate the microscale RVE, i.e.,

$$d = 1. \quad (32)$$

The final form of the fracture model (31) is rather concise involving additive contributions of a strain-related term, a strain gradient-related term and strain rate-related term. It is worth mentioning that all these terms are not introduced through phenomenological assumptions. They are rigorously derived from the two-scale asymptotic analysis. The coefficients of these terms are expressed by derivatives of tensor functions \mathbf{C} , \mathbf{D} and \mathbf{F} which can be calculated by integrals of first order cell solutions. The only inputs for constructing the fracture model are micro-crack distribution and Griffith law for single micro-crack propagation. Equipped with the micro-crack growth Eq. (31) and macro fracture criterion (32), we can predict fracture of macro structures accounting for micro-crack evolutions. If the strain rate term and the dependence of G_c on \dot{d} are neglected, the model is reduced to the fracture criterion obtained in the earlier work of the authors for quasi-static loading (Rao et al., 2022).

We remark here that Keita et al. (2014) has used a different two-scale analysis procedure to model dynamic brittle fracture. Distinctions between the present work and Keita et al. (2014) lie in several aspects. Firstly, we approximate the strain energy density, instead of the J-integral as in Keita et al. (2014), by the two-scale asymptotic expansion theory. Secondly, the novel fracture model in the present work involves strain gradient effects, which are absent in Keita et al. (2014). Thirdly, the strain rate effects are treated in different manner. In Keita et al. (2014), the dynamic energy release rate is finally approximated by the semi-analytical relation $G^{\text{dy}} \approx (1 - v/C_R) G^{\text{stat}}$ (where C_R is the Rayleigh wave velocity and G^{stat} is the energy release rate for quasi-static condition) which leads to elimination of the strain rate term. Nevertheless, in the present work, G^{dy} is accurately calculated through the micromechanical first-order cell solutions and a strain rate term is explicitly involved.

4. Application and validation

4.1. Construction functions \mathbf{C} , \mathbf{D} , \mathbf{F} and their derivatives

Coefficients of the micro-crack growth Eq. (31) are expressed in form of derivatives of the tensor valued functions $\mathbf{C}(d)$, $\mathbf{D}(d)$, $\mathbf{F}(d)$. Before conducting numerical analysis on material and structure responses, we prepare these functions and their derivatives by using first order cell solutions. We firstly calculate the values of $C_{ijkl}(d)$, $D_{pqjmn}(d)$ and $F_{ijkl}(d)$ at discrete points: $d = 0, 0.01, 0.02, \dots, 0.99, 0.991, 0.992, \dots, 0.999$ in interval $(0, 1)$. For each discrete point of d , the first order cell solutions $\mathbf{N}^{pq}(\mathbf{y})$ are obtained by using finite element simulations on the microscale RVE, see details in Rao et al. (2022). Then C_{ijkl} , D_{pqjmn} and F_{ijkl} at the discrete points are calculated by integrals according to Eqs. (19), (21) and (25). After the tensor function values at the discrete points are calculated, we construct the continuous functions $C_{ijkl}(d)$, $D_{pqjmn}(d)$ and $F_{ijkl}(d)$ by using cubic spline interpolation.

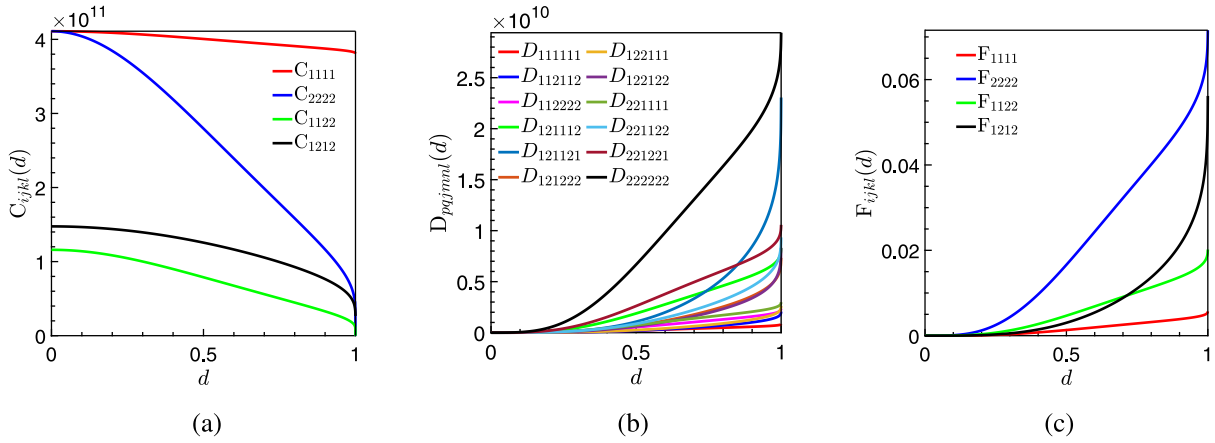


Fig. 3. (a) $C_{ijkl} - d$ curve; (b) $D_{pqjmn} - d$ curve; (c) $F_{ijkl} - d$ curve.

And the derivatives $C'_{ijkl}(d)$, $D'_{pqjmn}(d)$ and $F'_{ijkl}(d)$ are calculated as derivatives of the corresponding cubic spline interpolation functions.

The calculated $C_{ijkl}(d)$ function for plain strain problem is displayed in Fig. 3(a). $C_{ijkl}(0)$ equals the matrix modulus for materials free of micro-crack, that is $C_{1111}(0) = C_{2222}(0) = E(1 - \nu)/(1 - 2\nu)(1 + \nu)$, $C_{1122}(0) = C_{2211}(0) = E\nu/(1 - 2\nu)(1 + \nu)$, $C_{1212}(0) = E/2(1 + \nu)$. Due to the symmetry of $N^{pq}(\mathbf{y})$ (see details in Rao et al. (2022)), $C_{1112} = C_{1222} \equiv 0$ and they are not shown. All the non-zero components C_{ijkl} decrease as d increases. Different from the widely used phenomenological linear assumption $C_{ijkl}(d) = (1 - d)a_{ijkl}$ (Gross and Seelig, 2017), the present model predict obvious nonlinearity in the relation between macroscale effective modulus and the micro-crack variable. As d increases, the elastic resistance C_{2222} along the direction vertical to the micro-crack decreases most remarkably while the elastic resistance C_{1111} along the direction parallel to the micro-crack decreases most slightly.

Fig. 3(b) shows the components of tensor \mathbf{D} as functions of d . According to the symmetry and anti-symmetry of the first-order cell solutions with respect to the middle planes, the sixth-order tensor \mathbf{D} only has 12 non-zero components (see details in Rao et al. (2022)). Contrary to the homogenized elastic tensor C_{ijkl} , all components D_{pqjmn} increase as d increases. It means that strain gradients have no influence on the strain energy U for homogeneous material and gradient effects become more significant as d increases. This feature is consistent with results obtained in the literature (Barboura and Li, 2018; Yang et al., 2022). From (30), we find that the strain gradient term can reduce the dynamic energy release rate G^{dy} , which indicates that increasing in strain gradient inhibits micro-crack propagation. Fig. 3(c) shows the non-zero components of tensor \mathbf{F} as a function of d . It is shown that all components F_{ijkl} increase as d increases and all the nonzero components approaches 0 as d approaches 0. Similar to the strain gradient term, the strain rate term makes negative contribution to the energy release rate G^{dy} in (30). As a result, we can expect higher strength for higher strain rate.

4.2. Numerical implementation algorithm

We implement the model into an explicit Lagrangian finite element code. Then we apply the present model to investigate dynamic fracture of brittle materials under different loading conditions, focusing on combining influences of microstructural size, strain gradient and strain rate.

Macro structures are discretized into triangle elements. To exhibit effects of strain gradient, the Lagrangian P_2 element is adopted for displacement variable \mathbf{u} , while P_0 (piece-wise constant) integration is adopted for damage variable d . At time step $t^{n+1} = t^n + \Delta t$, with known

Algorithm 1 Numerical algorithm for updating d^{n+1} .

- 1: Set $d = d^n$;
- 2: Calculate $G^{dy}(d) = -\frac{\varepsilon}{2} C'_{ijkl}(d) \varepsilon_{ij} \varepsilon_{kl} - \frac{\varepsilon^3}{2} D'_{pqjmn}(d) \varepsilon_{pq,j} \varepsilon_{mn,l} - \frac{\varepsilon^3}{2} \rho F'_{pqmn}(d) \dot{\varepsilon}_{pq} \dot{\varepsilon}_{mn}$, where $\mathbf{C}'(d)$, $\mathbf{D}'(d)$, $\mathbf{F}'(d)$ are calculated by cubic spline interpolations (detailed in Section 4.1);
- 3: If $G^{dy} > G_c(0)$:
- 4: Calculate d by solving $G_c\left(\frac{\varepsilon(d - d^n)}{2\Delta t}\right) = G^{dy}$;
- 5: $d^{n+1} = d$;
- 6: Return.

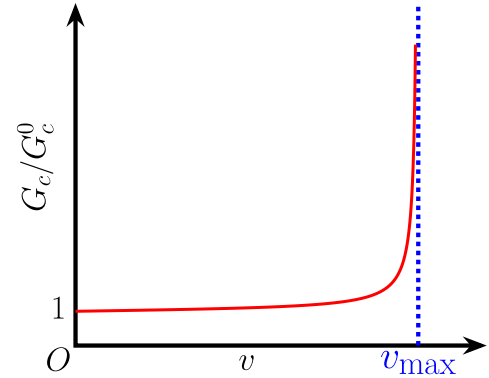


Fig. 4. Typical dependence of fracture resistance G_c on crack-tip speed v .

displacement field, the strain ε_{ij}^{n+1} , strain gradient $\varepsilon_{ij,k}$ and strain rate $\dot{\varepsilon}_{ij}^{n+1} = \frac{\varepsilon_{ij}^{n+1} - \varepsilon_{ij}^n}{\Delta t}$ are firstly calculated at each element centroid. Then d^{n+1} for each element is updated according to the procedure displayed in Algorithm 1.

4.3. $G_c(v)$ and material parameters

The dynamic critical energy release rate $G_c(v)$ is material-dependent. Generally, $G_c(v)$ is an increasing function with $G_c(0) = G_c^0$ being the quasi-static critical energy release rate when inertia effects are neglected (Gross and Seelig, 2017). A typical figure for $G_c(v)$ is shown in Fig. 4, indicating that crack velocity-sensitivity of G_c increases as v increases (Gross and Seelig, 2017). For the growth of mode-I crack, the crack-tip speed is limited by the Rayleigh wave speed C_R , which can

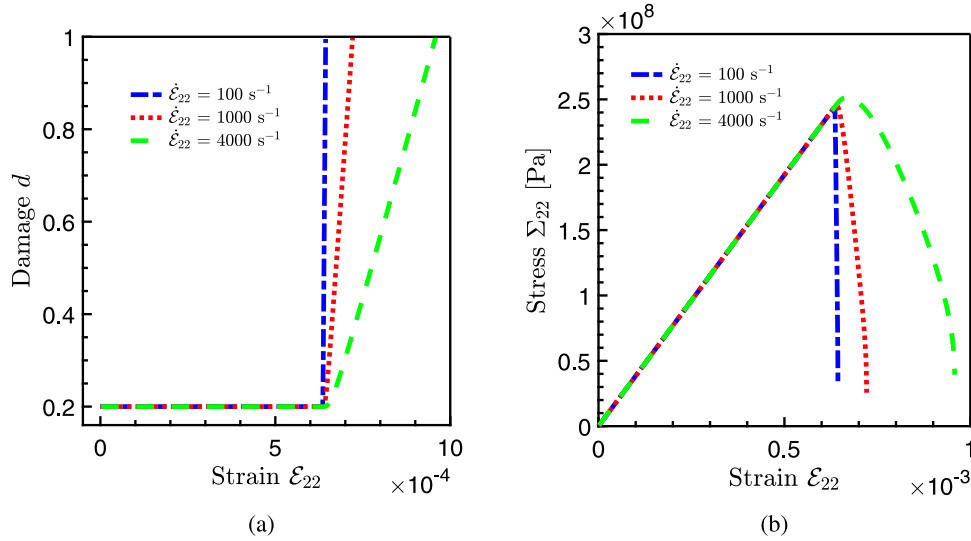


Fig. 5. Effects of strain rate $\dot{\epsilon}_{22}$ on (a) damage evolution and (b) stress-strain relation, with $\epsilon = 1 \times 10^{-3} \text{ m}$ and initial damage $d_0 = 0.2$.

Table 1

Material parameters for AL23 alumina and PMMA.

Material	E (GPa)	ν (-)	G_c^0 (J/m ²)	ρ (kg/m ³)
AL23 alumina	360	0.22	50.752	3890
PMMA	3.24	0.35	350	1190

be approximated as (Freund, 1998)

$$C_R \approx \frac{0.862 + 1.14\nu}{1 + \nu} \sqrt{\frac{E}{2\rho(1 + \nu)}},$$

where ν is the Poisson ratio and E is the Young's modulus. Here, we adopt the following function form for $G_c(v)$:

$$G_c(v) = G_c^0 \left(1 + \lambda \tan \left(\frac{\pi v}{2C_R} \right) \right). \quad (33)$$

In following calculations we take $\lambda = 0.1$. This choice can produce a limit speed $v_{\max} = C_R$ for mode-I crack as shown in Fig. 4 since the energy release rate vanishes for $v > C_R$ (Gross and Seelig, 2017). Note that more accurate $G_c(v)$ function can be determined for specific materials by experiments. This topic is beyond the main purpose of the present work. The main contribution of the present work is the strain gradient and strain rate effects on the left side of the expression (31), independent of specific $G_c(v)$. More accurate form $G_c(v)$ may be used in future applications of the present model.

In following simulations, material parameters for two typical brittle materials, AL23 alumina (Zinszner et al., 2015) and PMMA (polymethylmethacrylate) (Dascalu, 2018) are used, as listed in Table 1.

4.4. Local macro mechanical responses

In this subsection, we test local mechanical responses of a single macro material point, i.e., a Gaussian point in finite element simulations. The material parameters for AL23 alumina are used. We focus on mechanical responses under uniaxial tension: all the components of macro strain ϵ are set to be zero except $\epsilon_{22} = \dot{\epsilon}_{22}t$, where $\dot{\epsilon}_{22}$ is the constant strain rate and t is time. Damage d are updated according to Algorithm 1 at each time step.

Fig. 5 displays the predicted strain rate effects on damage evolution and stress-strain relation, when $\epsilon = 1 \times 10^{-3} \text{ m}$ and initial damage $d_0 = 0.2$. The curves at lower strain rate 100 s^{-1} exhibit typical brittle fracture characteristics, i.e., damage sharply increases and stress sharply drops when the strain reaches a critical value. At higher strain rates, material ductility increases in the sense that micro-crack propagates

and stress drops in a much slower manner. The stress-strain curve in Fig. 5(b) shows that higher strain rate leads to higher fracture strength (maximum tensile stress, denoted as Σ_{\max}), which is consistent with widely known strain rate hardening effects (Bischoff and Perry, 1991). From Eq. (31), we find that the strain rate term is coupled with ϵ^3 . This indicates that strain rate sensitivity is strongly related to ϵ . Larger ϵ would result in more significant strain rate effect. For this reason, we have conducted other calculations with larger $\epsilon = 5 \times 10^{-3} \text{ m}$, 5 times of the ϵ in Fig. 5. The results are presented in Fig. 6. Comparing Figs. 5 and 6, it is confirmed that strain rate sensitivity of fracture behaviors is higher for larger microstructural length ϵ . From the present model, the physical origin of strain rate hardening effect is that the strain rate term in (30) makes negative contribution to the micro-crack energy release rate G^{dy} and thus retard the micro-crack propagation. In addition to the fracture strength, both toughness (the area below the stress-strain curve) and ductility (measured by the strain at fracture) are enhanced as strain rate increases.

Fig. 7 displays effects of microstructural length scale ϵ on tensile responses at constant strain rate $\dot{\epsilon}_{22} = 1 \times 10^3 \text{ s}^{-1}$ with initial damage $d_0 = 0.2$. From Fig. 7(a), it is shown that growth of d begins at larger strain for larger ϵ , indicating that the critical strain at which micro-crack starts to propagate is sensitive to microstructural length scale ϵ . Toughness and ductility of material both decrease as ϵ increases.

To more quantitatively reveal coupling effects of microstructural length and strain rate, we display $\Sigma_{\max} - \epsilon$ relations under different strain rate in Fig. 8(a) and $\Sigma_{\max} - \dot{\epsilon}_{22}$ relations with different ϵ in Fig. 8(b). From Fig. 8(a), it is shown that the microstructural length dependence of fracture strength Σ_{\max} generally exhibits Hall-Petch relations, i.e., Σ_{\max} linearly relates to $1/\sqrt{\epsilon}$. For strain rate $\dot{\epsilon}_{22} \leq 10^3 \text{ s}^{-1}$, the $\Sigma_{\max} - \epsilon$ curves under different strain rates almost coincide with slope about $1.1 \text{ GPa m}^{1/2}$. The $\Sigma_{\max} - \epsilon$ curve for higher strain rate 10^4 s^{-1} deviates obviously from the cases of lower strain rates, with slope about $1.0 \text{ GPa m}^{1/2}$. From Fig. 8(b), nonlinearity of strain rate dependence of fracture strength is only obvious at the lower end of strain rate. The $\Sigma_{\max} - \dot{\epsilon}_{22}$ curves in higher strain rate regime are approximately linear. For example, in the case of $\epsilon = 0.005 \text{ m}$, the curve is nearly linear for $\dot{\epsilon} > 2000 \text{ s}^{-1}$. From Fig. 8(b), it is also confirmed that the strain rate sensitivity (the slope of the curves) increases as ϵ increases, consistent with results in Figs. 5 and 6.

Fig. 9 displays effects of strain gradient on tensile responses, when $\dot{\epsilon}_{22} = 2 \times 10^3 \text{ s}^{-1}$, $\epsilon = 5 \times 10^{-3} \text{ m}$ and $d_0 = 0.2$. It is shown that the critical strain at which micro-crack starts to grow increases as strain gradient $\dot{\epsilon}_{22}$ increases. Toughness, ductility and fracture strength all increase as strain gradient increases. This is due to that strain gradient term

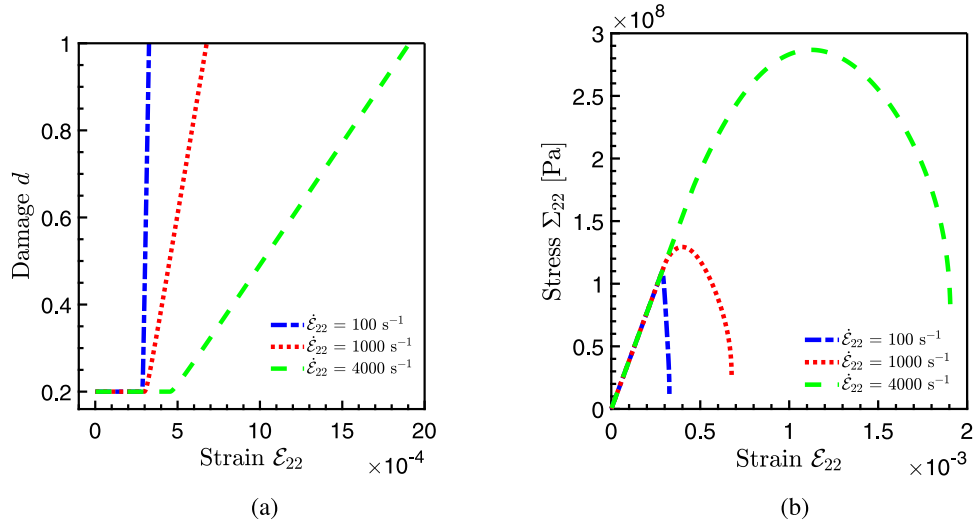


Fig. 6. Effects of strain rate $\dot{\epsilon}_{22}$ on (a) damage evolution and (b) stress-strain relation, with $\epsilon = 5 \times 10^{-3} \text{ m}$ and initial damage $d_0 = 0.2$.

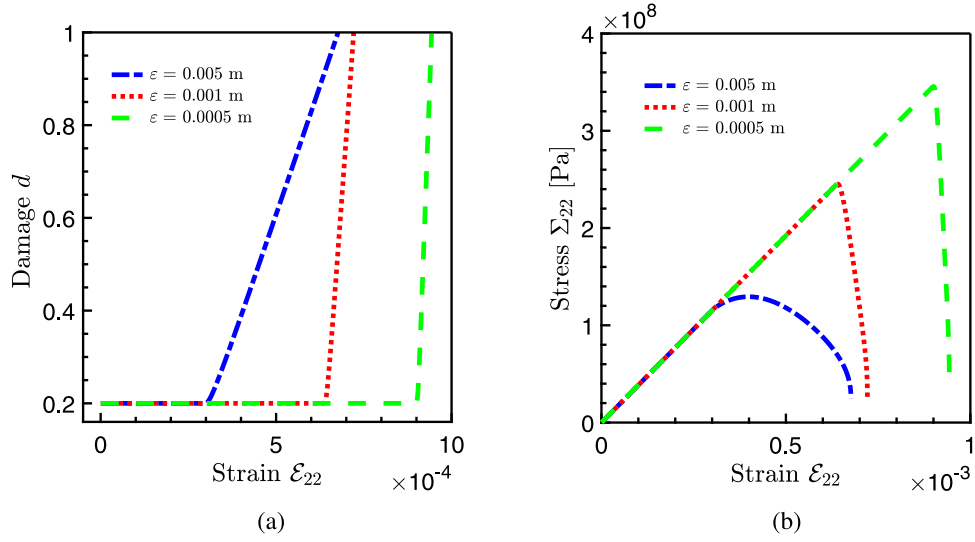


Fig. 7. Effects of ϵ on (a) damage evolution and (b) stress-strain relation, with $\dot{\epsilon}_{22} = 1 \times 10^3 \text{ s}^{-1}$ and initial damage $d_0 = 0.2$.

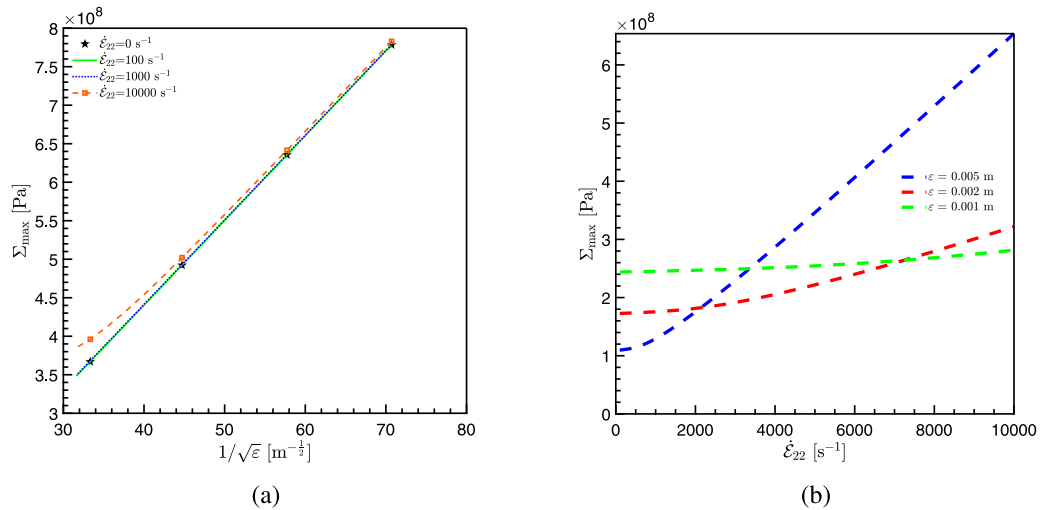


Fig. 8. (a) Dependence of fracture strength on ϵ under different strain rate; (b) Dependence of fracture strength on strain rate with different ϵ . The results are calculated with $d_0 = 0.2$.

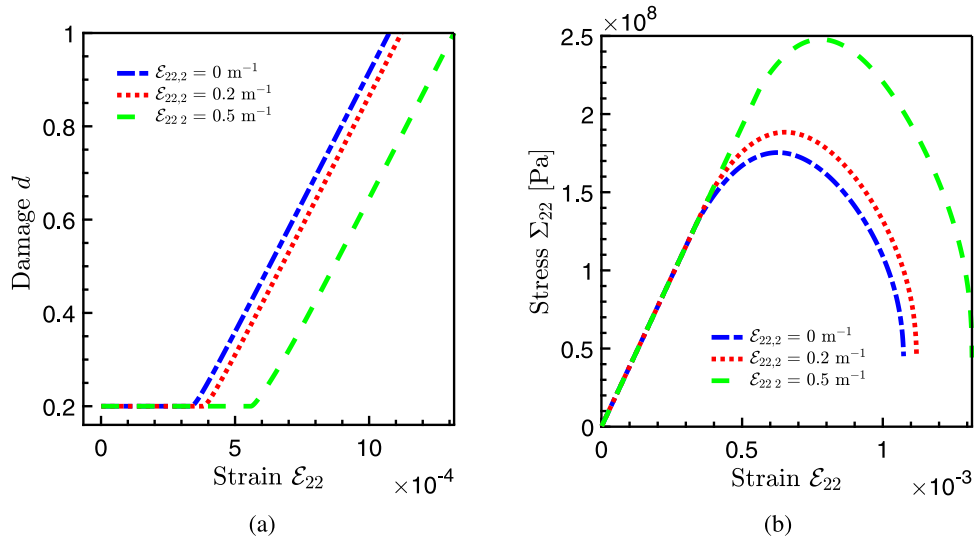


Fig. 9. Effects of strain gradient $\epsilon_{22,2}$ on (a) damage evolution and (b) stress-strain relation, with $\dot{\epsilon}_{22} = 2 \times 10^3 \text{ s}^{-1}$, $\epsilon = 5 \times 10^{-3} \text{ m}$ and $d_0 = 0.2$.

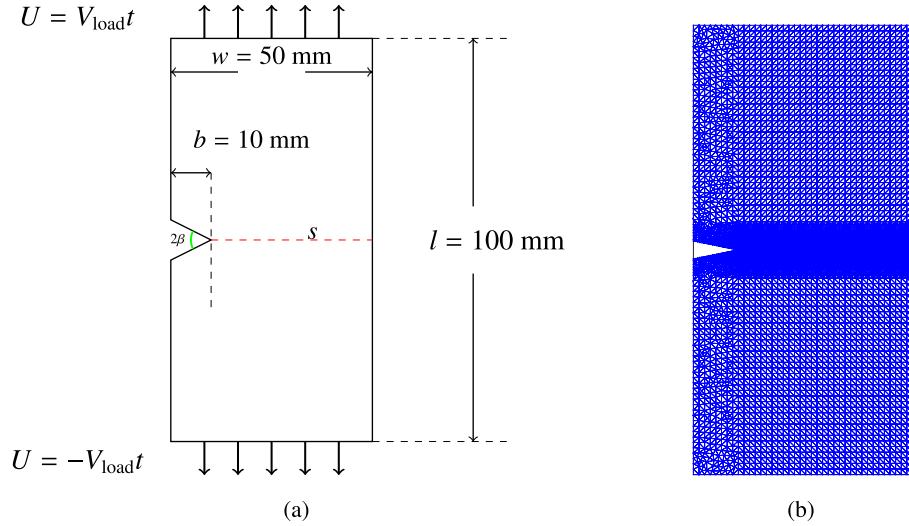


Fig. 10. Tensile simulation for a V-notch plate: (a) geometry and boundary conditions; (b) FEM mesh.

makes negative contribution to the micro-crack energy release rate G^{dy} as in Eq. (30). Note that, from Eq. (30), strain rate and strain gradient are not coupled in the energy release rate formulation. Thus, the strain gradient dependence of fracture behaviors is not sensitive to strain rate. More quantitative results on coupled effects of microstructure length and strain gradient can be found in the previous work of the authors (Rao et al., 2022).

4.4.1. Crack propagation in a V-notch plate

In this subsection, we present simulation results of a rectangular PMMA plate of $0.1 \text{ m} \times 0.05 \text{ m}$ that contains a V-notch with depth $b = 0.01 \text{ m}$ and opening angle $\beta = \arctan 1/5$, as illustrated in Fig. 10(a). In the simulations, the loading velocity V_{load} ranges from 1 m/s to 40 m/s . Time step is set to $\Delta t = 2 \times 10^{-7} \text{ s}$. Considering the symmetry of the geometric configuration with respect to the central axis s , symmetrical mesh for the plate is adopted. And the mesh is refined in the expected crack propagation zone as shown in Fig. 10(b).

We use different element sizes $h = 0.47, 0.31, 0.18, 0.12 \text{ mm}$ near the central line s to investigate the influence of the finite element mesh size. Fig. 11 shows the calculated fracture zones with loading velocity $V_{\text{load}} = 40 \text{ m/s}$. Crack branching is observed in the simulations. The damage fracture zones are similar in all the four cases, indicating

insensitivity of calculated fracture zone to mesh size. In addition, from the stress-displacement curves shown in Fig. 12, we find that the two curves calculated with small mesh sizes $h = 0.18 \text{ mm}$ and $h = 0.12 \text{ mm}$ show subtle differences, indicating that the calculation results tend to converge as the mesh size decreases, which further verifies the mesh insensitivity.

Fig. 13 displays the stress-displacement curve for four different loading speeds. It is shown that the ductility increases as V_{load} increases and the critical stress is higher for larger V_{load} , this is consistent with the local material responses analyzed in Section 4.4. It is the result of kinetics of energy barriers and inertia effects in the vicinity of a running crack (Reinhardt and Weerheijm, 1991).

Fig. 14 displays the fracture zone for four loading velocities $V_{\text{load}} = 1 \text{ m/s}, 10 \text{ m/s}, 20 \text{ m/s}, 40 \text{ m/s}$ with element size $h = 0.12 \text{ mm}$. The crack bifurcation was observed for all loading velocities V_{load} . It is shown that the bifurcation point of crack appears earlier for higher strain rate (loading velocity), indicating that high strain rate promotes the crack branching. Similar numerical results have been obtained by Dascalu (2018).

Fig. 15 compares the stress-displacement curves calculated based on the model Eq. (31) and the model when strain gradient term is ignored under $V_{\text{load}} = 40 \text{ m/s}$. The microstructure parameter is set to

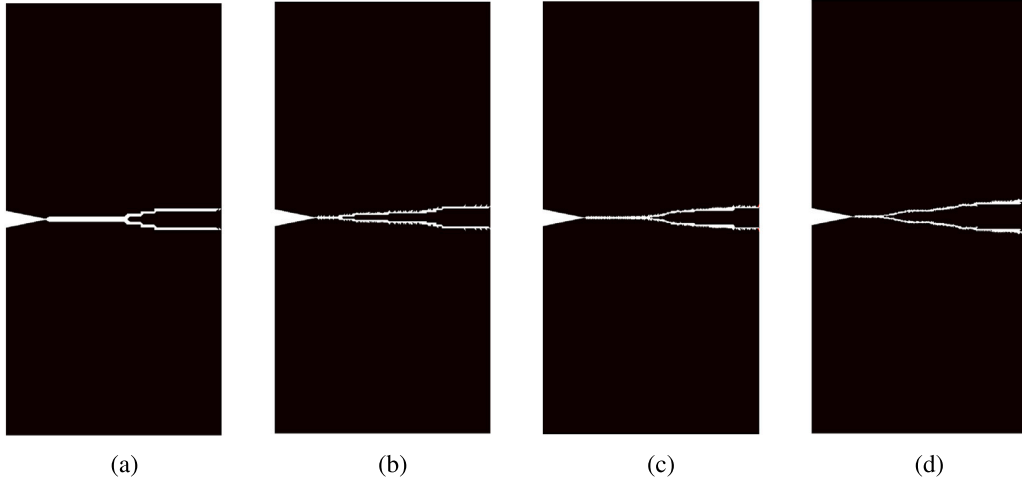


Fig. 11. Calculated fracture zones for different mesh sizes in the case of $V_{\text{load}} = 40$ m/s: (a) $h = 0.47$ mm; (b) $h = 0.31$ mm; (c) $h = 0.18$ mm; (d) $h = 0.12$ mm.

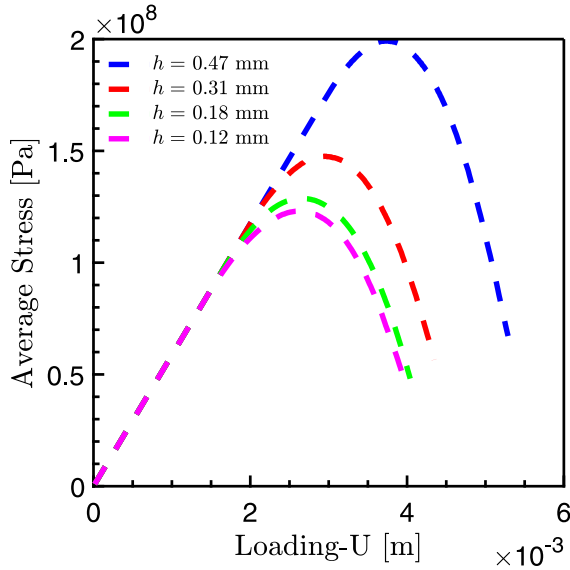


Fig. 12. Stress-Displacement curve of $V_{\text{load}} = 40$ m/s for different meshes.

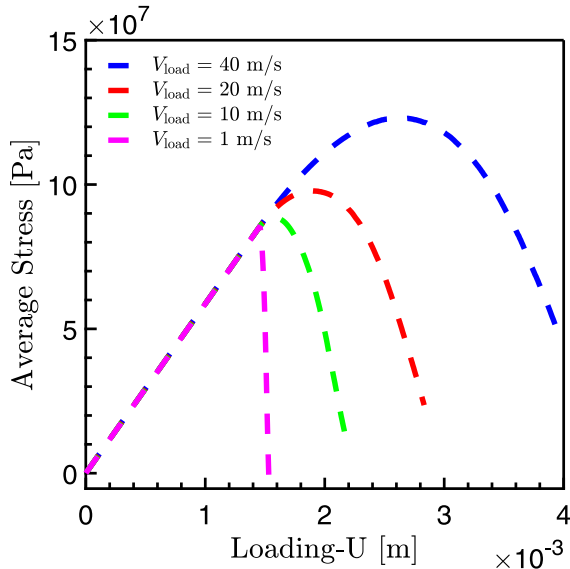


Fig. 13. Stress-Displacement curve for different loading velocities.

$\varepsilon = 0.5$ mm, large enough to illustrate strain gradient effect. It is shown that involving strain gradient effects enhance the calculated ductility and the critical loading stress. In the initial stage when the macro-crack is stable, the two curves in Fig. 15 coincides. The strain gradient effect becomes noticeable when the macro-crack begins to grow at $U \approx 1.3 \times 10^{-3}$ m.

4.4.2. Spalling fracture

Spalling (or spall, spallation, scabbing, or by other names) is a typical dynamic tensile rupture phenomenon that has a long research history (Antoun et al., 2003). Spalling experiments have become a standard way to probe dynamic material properties under extremely high strain rates. Spall experiments are typically performed by plate impact. A general plate-impact set-up contains a flyer and a target, as illustrated in Fig. 16. Impacting generates shock compression waves propagating into both the flyer and target. Reflection of the compression waves at free surfaces generates rarefaction waves which propagates back into the flyer and target. Superposition of the two reflected rarefaction waves results in tensile stress. When tensile stress exceeds fracture strength, spalling fracture occurs. The stress waves in spalling experiments can also be induced through an electromagnetic device rather than impact. The electromagnetic technique allows for the generation of a more controlled stress wave and leads to “shockless” spalling as stated in Zinszner et al. (2015). As impact-induced intense fragmentation of brittle materials brings extra difficulties in probing dynamic material responses, the electromagnetic loading-induced shockless spalling is particularly suitable for investigating dynamic properties of brittle materials such as alumina ceramic under high strain rate.

Here, we carry out numerical simulations on shockless spalling tests, in comparison with a series of experiments performed on an AL23 ceramic using electromagnetic loading (Zinszner et al., 2015). Generally, in experiments, the lateral dimension of the sample is much larger than the sample thickness. Thus, deformation of materials near the central axis is well approximated by uniaxial strain problem (Xiang et al., 2021). As a result, in numerical simulation, a simplified geometry can be adopted as illustrated in the dotted box in Fig. 16. Only a part of the samples near the central axis is selected for numerical simulation. The zero radial displacement boundary condition is applied on the two sides of the selected region and the top boundary remains free to move to mimic a uniaxial strain loading. In the simulations, stress wave is induced by prescribing velocity boundary conditions at the bottom of the sample. Similar simulation set-up was adopted in Simons et al. (2019). Four different loading velocity–time curves are tested as shown in Fig. 17, corresponding to the four loading conditions of the experiments in Zinszner et al. (2015).

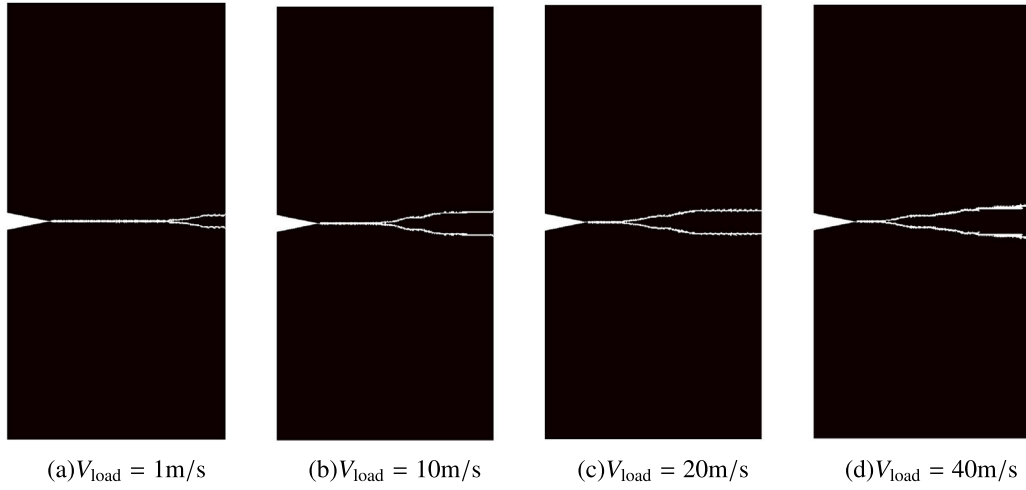


Fig. 14. Fracture zone for different loading velocities.

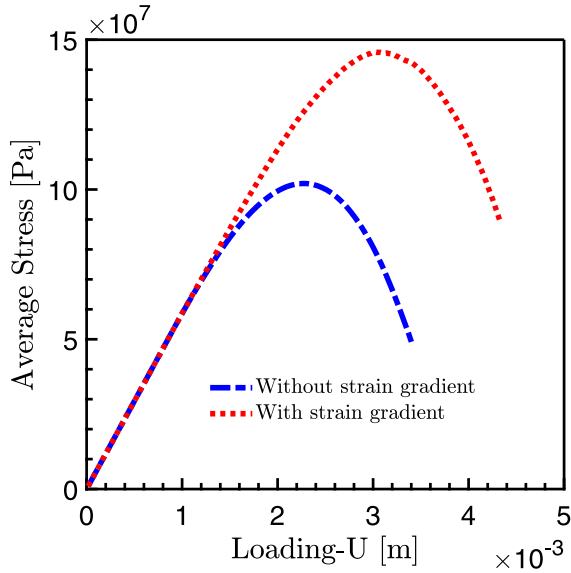


Fig. 15. Effect of strain gradient for stress-displacement curve.

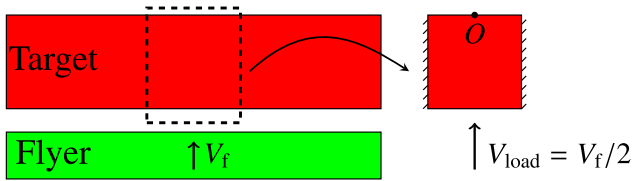


Fig. 16. The plate-impact experiments and simplified model: the problem can be simplified to a column of material as shown in the dotted box.

The material parameters for AL23 alumina are used in the simulations, as listed in Table 1. The target plate is set as a 10 mm long and 2 mm wide. The mesh size is set to $h \approx 0.1$ mm. Note that, ϵ and initial damage d_0 are inputs for our model. They have clear physical meaning and can be determined by experimental diagnostic techniques such as electron back scattering diffraction. However, when quantitatively comparing our simulations with experiments in Zinszner et al. (2015), we have to calibrating ϵ and d_0 because these microstructural parameters for experimental samples are not available in the experimental report.

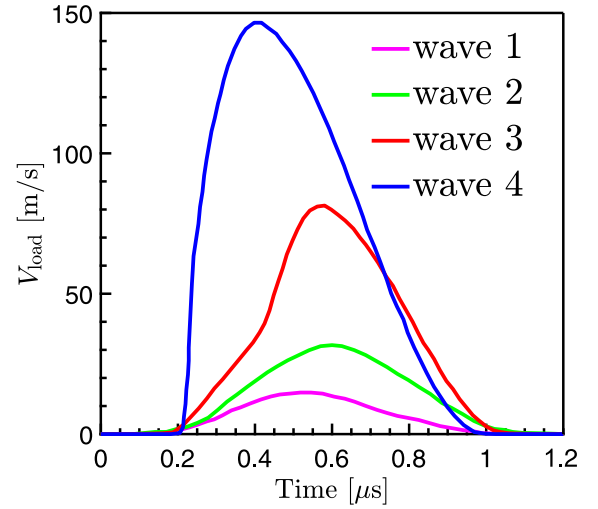


Fig. 17. Loading velocity history for inducing stress waves in the spall simulations.

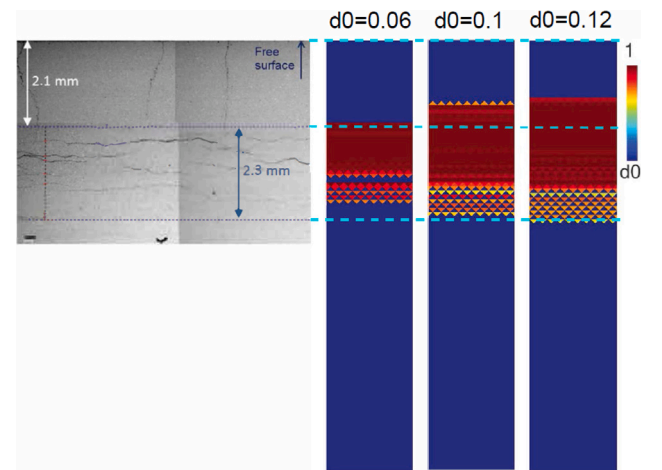


Fig. 18. Comparing calculated fracture zones with experiments (Zinszner et al., 2015).

Fig. 18 displays fracture zones with different $d_0 = 0.06, 0.1$, and 0.12 and fixed $\epsilon = 0.8$ mm by applying wave 1 shown in Fig. 17. Here,

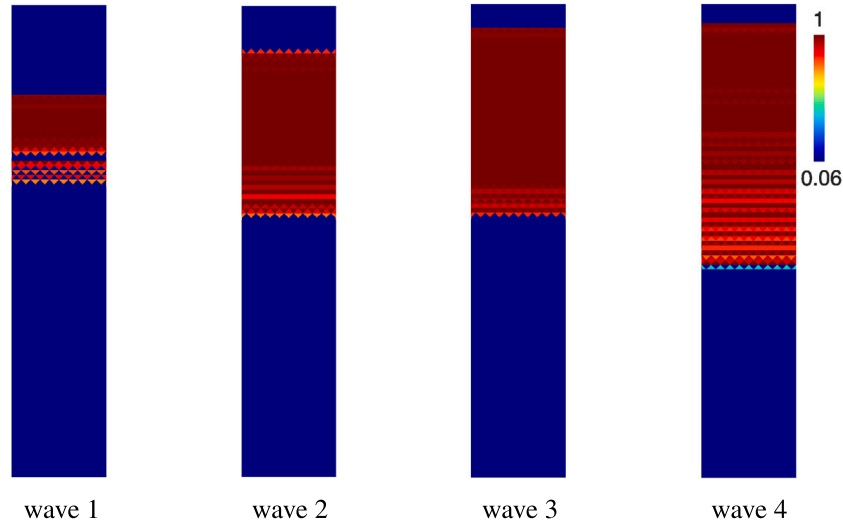


Fig. 19. Fracture zones obtained by applying different stress waves.

the label variable d_0 for colorbar is the initial damage. It is observed that the calculated fracture zone for $d_0 = 0.06$ agrees well with the experiment. Especially, the damaged zone is about 2.1 mm away from the free surface. The maximum distance between the damaged zone and the free surface is about 4.4 mm for all three simulations, which is quantitatively consistent with the experimental result.

Fig. 19 displays calculated fracture zone with initial damage $d_0 = 0.06$ and microstructure parameter $\epsilon = 0.8$ mm by applying the four stress waves as shown in Fig. 17. It is shown that the size of the damaged zone is strongly dependant on the strain-rate. As strain rate increases, the maximum distance between the damaged zone and the free surface increases while the minimum distance between the damaged zone and the free surface decreases. The damaged zone is larger for higher strain rate.

In experiments, it is generally difficult to measure data such as pressure, damage distribution inside the shocked target. And rear free surface velocity profile is one of the most often measured quantities. Dynamic materials properties (such as Hugoniot yield limit, spall strength etc.) are deduced from free surface velocity profiles. Free surface velocity can be measured by capacitor gauge, electromagnetic gauge and laser Doppler techniques (see a review in Antoun et al. (2003)). In our simulations, velocity histories of the central point O (as illustrated in Fig. 16) at the rear surface is recorded and compared to experimental results.

Fig. 20 displays the comparisons between calculated free surface velocity profiles with experimental results under the series of loading conditions displayed in Fig. 17. The dashed lines with superscript “exp” are the experimental results obtained in Zinszner et al. (2015) and the dashed lines with superscript “sim” are simulation results in the present work. The numerical results shown in Fig. 20 are obtained by taking $\epsilon = 0.8$ mm for all the four simulations and taking $d_0 = 0.06, 0.06, 0.15, 0.12$ for wave 1, wave 2, wave 3 and wave 4 respectively. It is shown that the calculated results closely reproduce experimental measurements. The subtle discrepancies may be attributed to randomness and complexity of microstructure distribution in experimental samples and natural uncertainties in experimental diagnostic techniques.

To further validate the model, in Fig. 21, we compare calculated spall strengths with experimental results measured in another series of spalling fracture experiments by Erzar and Buzaud (2012). Spall strength increases as strain rate increases. The calculated spall strength as a function of strain rate agrees well with the experimental results in the case of $\epsilon = 1$ mm and $d_0 = 0.08$. The parametric investigations show that the effect of strain rate on spall strength is more sensitive for larger ϵ when d_0 is fixed. While the effect of d_0 on fracture strength σ_{spall} is not sensitive to strain rate for fixed microstructure parameter ϵ .

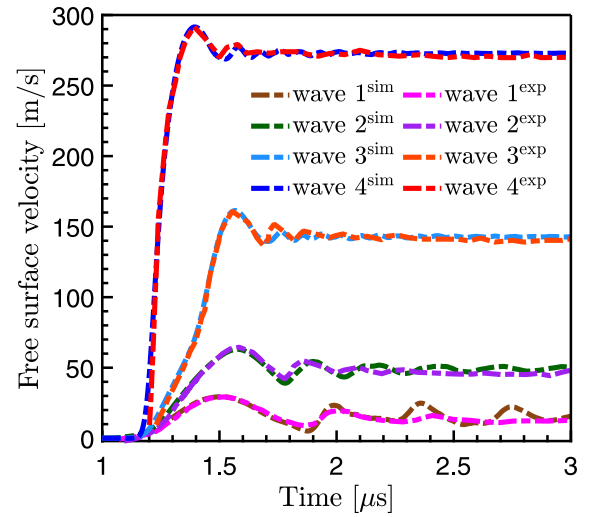


Fig. 20. Comparisons of calculated free surface velocity profiles with experimental measurements.

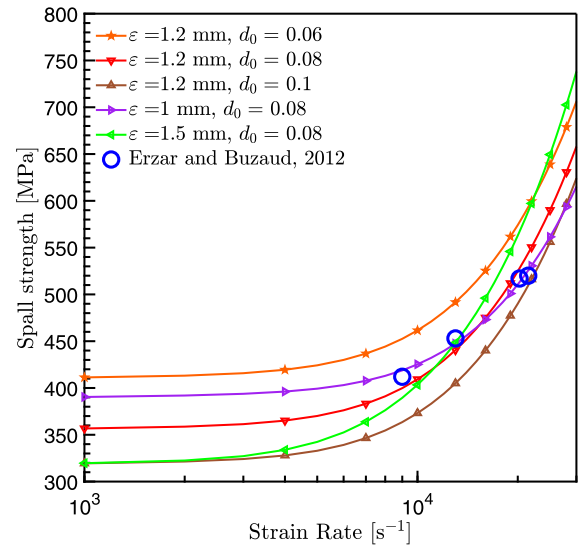


Fig. 21. Comparisons of calculated spall strengths with experimental measurements in Erzar and Buzaud (2012).

5. Conclusion

By adding micro-inertia effect into the energy-based two-scale asymptotic theory (Rao et al., 2022), the present work unifies microstructural length scale, strain gradient and strain rate effects on fracture. Provided known properties of a single micro-crack described by a Griffith law, no additional phenomenological *ad hoc* hypotheses are introduced. Microstructural length scale, strain gradient and strain rate effects on fracture are all natural consequences of the two-scale asymptotic expansion theory.

The local energy release rate of micro-crack based on the two-scale theory is an analytical formulation involving additive contributions of macro strain, strain gradient and strain rate. The coefficients of these terms are obtained by derivatives of tensor functions which are expressed by integrals of first order cell solutions. Normalized micro-crack length (d) is viewed as a measurement of macro damage. Macro fracture is identified when $d = 1$.

Although the physical hypothesis of the model is simple, predictive capability of the model is inspiring. In the model, both the strain gradient term and the strain rate term make negative contributions to local energy release rate of micro-crack. Therefore, the model predicts that increasing in strain gradient or strain rate would result in enhancement of toughness, ductility and fracture strength. Moreover, both strain gradient and strain rate effects become more significant for larger microstructural size ϵ (micro-crack separation). Simulations on crack propagation in V-notch plate show that high strain rate facilitates macro crack branching. Based on the model, finite element simulations on spalling fracture of AL23 alumina well reproduce fracture zones, free surface velocity profiles and spall strengths measured in series of experiments.

The present work only considers mode-I crack opening of two-dimensional micro-crack. Efforts are being made by the authors to extend the model to three-dimensional problems. Extending the modeling approach to mixed mode micro-cracking problems may be more challenging and requires further endeavors.

Declaration of competing interest

The authors declare that they have no known competing financial interests or personal relationships that could have appeared to influence the work reported in this paper.

Data availability

Data will be made available on request.

Acknowledgments

The work is supported by the National Natural Science Foundation of China (No. 12272061, No. 51739007), Strategic Priority Research Program of the Chinese Academy of Sciences (No. XDC06030101).

References

- Antoun, T., Curran, D.R., Razorenov, S.V., Seaman, L., Kanel, G.I., Utkin, A.V., 2003. *Spall Fracture*. Springer New York.
- Barboura, S., Li, J., 2018. Establishment of strain gradient constitutive relations by using asymptotic analysis and the finite element method for complex periodic microstructures. *Int. J. Solids Struct.* 136, 60–76.
- Bischoff, P.H., Perry, S., 1991. Compressive behaviour of concrete at high strain rates. *Mater. Struct.* 24 (6), 425–450.
- Blanco, P.J., Sánchez, P.J., De Souza Neto, E.A., Feijóo, R.A., 2016a. The method of multiscale virtual power for the derivation of a second order mechanical model. *Mech. Mater.* 99, 53–67.
- Blanco, P.J., Sánchez, P.J., de Souza Neto, E.A., Feijóo, R.A., 2016b. Variational foundations and generalized unified theory of rve-based multiscale models. *Arch. Comput. Methods Eng.* 23 (2), 191–253.
- Brach, S., Hossain, M., Bourdin, B., Bhattacharya, K., 2019. Anisotropy of the effective toughness of layered media. *J. Mech. Phys. Solids* 131, 96–111.
- Chatzigeorgiou, G., Charalambakis, N., Murat, F., 2009. Homogenization of a pressurized tube made of elastoplastic materials with discontinuous properties. *Int. J. Solids Struct.* 46 (21), 3902–3913.
- Chen, J., Wei, Y., Huang, Y.T., Hutchinson, J., Hwang, K., 1999. The crack tip fields in strain gradient plasticity: the asymptotic and numerical analyses. *Eng. Fract. Mech.* 64 (5), 625–648.
- Chopin, J., Bhaskar, A., Jog, A., Ponson, L., 2018. Depinning dynamics of crack fronts. *Phys. Rev. Lett.* 121, 235501.
- Cioranescu, D., Donato, P., 1999. *An Introduction To Homogenization*, Vol. 17. Oxford university press Oxford.
- Dascalu, C., 2018. Multiscale modeling of rapid failure in brittle solids: branching instabilities. *Mech. Mater.* 116, 77–89.
- Dascalu, C., Bilbie, G., Agiasofitou, E.K., 2008. Damage and size effects in elastic solids: A homogenization approach. *Int. J. Solids Struct.* 45 (2), 409–430.
- De Souza Neto, E.A., Blanco, P.J., Sánchez, P.J., Feijóo, R.A., 2015. An rve-based multiscale theory of solids with micro-scale inertia and body force effects. *Mech. Mater.* 80, 136–144.
- Erzar, B., Buzaud, E., 2012. Shockless spalling damage of alumina ceramic. *Eur. Phys. J. Spec. Top.* 206 (1), 71–77.
- Fleck, N., Hutchinson, J., 1993. A phenomenological theory for strain gradient effects in plasticity. *J. Mech. Phys. Solids* 41 (12), 1825–1857.
- Fleck, N., Hutchinson, J., 2001. A reformulation of strain gradient plasticity. *J. Mech. Phys. Solids* 49 (10), 2245–2271.
- Freund, L.B., 1998. *Dynamic Fracture Mechanics*. Cambridge University Press.
- Gao, H., Huang, Y., Nix, W., Hutchinson, J., 1999. Mechanism-based strain gradient plasticity. *J. Mech. Phys. Solids* 47 (6), 1239–1263.
- Gao, H., Rice, J.R., 1989. A first-order perturbation analysis of crack trapping by arrays of obstacles. *J. Appl. Mech.* 56 (4), 828–836.
- Gilath, I., Eliezer, S., Dariel, M.P., Kornblit, L., 1988. Brittle-to-ductile transition in laser-induced spall at ultrahigh strain rate in 6061-T6 aluminum alloy. *Appl. Phys. Lett.* 52 (15), 1207–1209.
- Grady, D., 1988. The spall strength of condensed matter. *J. Mech. Phys. Solids* 36 (3), 353–384.
- Gross, D., Seelig, T., 2017. *Fracture Mechanics: With an Introduction To Micromechanics*. Springer.
- Hossain, M., Chatzigeorgiou, G., Meraghni, F., Steinmann, P., 2015. A multi-scale approach to model the curing process in magneto-sensitive polymeric materials. *Int. J. Solids Struct.* 69, 34–44.
- Hossain, M., Hsueh, C., Bourdin, B., Bhattacharya, K., 2014. Effective toughness of heterogeneous media. *J. Mech. Phys. Solids* 71, 15–32.
- Huang, Y., Gao, H., Nix, W., Hutchinson, J., 2000. Mechanism-based strain gradient plasticity. *J. Mech. Phys. Solids* 48 (1), 99–128.
- Hutchinson, J., Fleck, N., 1997. Strain gradient plasticity. *Adv. Appl. Mech.* 33, 295–361.
- Jarmakani, H., Maddox, B., Wei, C.T., Kalantar, D., Meyers, M.A., 2010. Laser shock-induced spalling and fragmentation in vanadium. *Acta Mater.* 58 (14), 4604–4628.
- Jiang, H., Huang, Y., Zhuang, Z., Hwang, K., 2001. Fracture in mechanism-based strain gradient plasticity. *J. Mech. Phys. Solids* 49 (5), 979–993.
- Keita, O., Dascalu, C., Francois, B., 2014. A two-scale model for dynamic damage evolution. *J. Mech. Phys. Solids* 64 (Mar.), 170–183.
- Kuliev, V.D., Morozov, E.M., 2016. The gradient deformation criterion for brittle fracture. *Dokl. Phys.* 61 (10), 502–504.
- Lam, D.C., Yang, F., Chong, A., Wang, J., Tong, P., 2003. Experiments and theory in strain gradient elasticity. *J. Mech. Phys. Solids* 51 (8), 1477–1508.
- Lazar, M., Maugin, G.A., Aifantis, E.C., 2006. Dislocations in second strain gradient elasticity. *Int. J. Solids Struct.* 43 (6), 1787–1817.
- Lazopoulos, K., 2004. On the gradient strain elasticity theory of plates. *Eur. J. Mech. A Solids* 23 (5), 843–852.
- Lebihain, M., Leblond, J.-B., Ponson, L., 2020. Effective toughness of periodic heterogeneous materials: the effect of out-of-plane excursions of cracks. *J. Mech. Phys. Solids* 137, 103876.
- Lebihain, M., Ponson, L., Kondo, D., Leblond, J., 2021. Effective toughness of disordered brittle solids: A homogenization framework. *J. Mech. Phys. Solids* 153, 104463.
- Lemaître, J., Chaboche, J.-L., 1994. *Mechanics of Solid Materials*. Cambridge University Press.
- Li, J., 2011. A micromechanics-based strain gradient damage model for fracture prediction of brittle materials - part I: Homogenization methodology and constitutive relations. *Int. J. Solids Struct.* 48 (24), 3336–3345.
- Li, M., Jiang, M., Li, G., He, L., Sun, J., Jiang, F., 2016. Ductile to brittle transition of fracture of a zr-based bulk metallic glass: Strain rate effect. *Intermetallics* 77, 34–40.
- Li, J., Pham, T., Abdelmoula, R., Song, F., Jiang, C., 2011. A micromechanics-based strain gradient damage model for fracture prediction of brittle materials - part II: Damage modeling and numerical simulations. *Int. J. Solids Struct.* 48 (24), 3346–3358.
- Li, Y., Zhou, M., 2013a. Prediction of fracture toughness of ceramic composites as function of microstructure: I. numerical simulations. *J. Mech. Phys. Solids* 61 (2), 472–488.

- Li, Y., Zhou, M., 2013b. Prediction of fracture toughness of ceramic composites as function of microstructure: II. analytical model. *J. Mech. Phys. Solids* 61 (2), 489–503.
- Liu, W., Gao, D., 2021. Hall-petch relation in the fracture strength of matrix-body pdc bits. *Int. J. Refract. Met. Hard Mater.* 98, 105537.
- Makvandi, R., Duczek, S., Juhre, D., 2019. A phase-field fracture model based on strain gradient elasticity. *Eng. Fract. Mech.* 220, 106648.
- Mindlin, R.D., 1965. Second gradient of strain and surface-tension in linear elasticity. *Int. J. Solids Struct.* 1 (4), 417–438.
- Mindlin, R.D., Eshel, N.N., 1968. On first strain-gradient theories in linear elasticity. *Int. J. Solids Struct.* 4 (1), 109–124.
- Mirkhalaf, M., Dastjerdi, A., Barthelat, F., 2014. Overcoming the brittleness of glass through bio-inspiration and micro-architecture. *Nature Commun.* 5 (3166).
- Nguyen, T.H., Niiranen, J., 2020. A second strain gradient damage model with a numerical implementation for quasi-brittle materials with micro-architectures. *Math. Mech. Solids* 25 (3), 515–546.
- Osovski, S., Srivastava, A., Ponson, L., Bouchaud, E., Tvergaard, V., Ravi-Chandar, K., Needleman, A., 2015. The effect of loading rate on ductile fracture toughness and fracture surface roughness. *J. Mech. Phys. Solids* 76, 20–46.
- Owen, D.M., Zhuang, S., Rosakis, A.J., Ravichandran, G., 1998. Experimental determination of dynamic crack initiation and propagation fracture toughness in thin aluminum sheets. *Int. J. Fract.* 90 (1–2), 153–174.
- Ozbolt, J., Sharma, A., Irhan, B., Sola, E., 2014. Tensile behavior of concrete under high loading rates. *Int. J. Impact Eng.* 69 (Jul.), 55–68.
- Peerlings, R., Fleck, N., 2004. Computational evaluation of strain gradient elasticity constants. *Int. J. Multiscale Comput. Eng.* 2 (4).
- Peerlings, R.R., de R RenéBorst, Brekelmans, W.M., de Jhp Henk Vree, 1996. Gradient enhanced damage for quasi-brittle materials. *Internat. J. Numer. Methods Engrg.* 39 (19), 3391–3403.
- Po, G., Lazar, M., Seif, D., Ghoniem, N., 2014. Singularity-free dislocation dynamics with strain gradient elasticity. *J. Mech. Phys. Solids* 68, 161–178.
- Rafiee, S., Gross, D., Seelig, T., 2004. The influence of microcrack nucleation on dynamic crack growth—a numerical study. *Eng. Fract. Mech.* 71 (4–6), 849–857.
- Ramanathan, S., Ertas, D., Fisher, D.S., 1997. Quasistatic crack propagation in heterogeneous media. *Phys. Rev. Lett.* 79, 873–876.
- Rao, Y., Xiang, M., Cui, J., 2022. A strain gradient brittle fracture model based on two-scale asymptotic analysis. *J. Mech. Phys. Solids* 104752.
- Ravi-Chandar, K., Yang, B., 1997. On the role of microcracks in the dynamic fracture of brittle materials. *J. Mech. Phys. Solids* 45 (4), 535–563.
- Reinhardt, H., Weerheijm, J., 1991. Tensile fracture of concrete at high loading rates taking account of inertia and crack velocity effects. *Int. J. Fract.* 51 (1), 31–42.
- Rittel, D., Maigre, H., 1996. An investigation of dynamic crack initiation in pmma. *Mech. Mater.* 23 (3), 229–239.
- Rocha, F.F., Blanco, P.J., Sánchez, P.J., de Souza Neto, E., Feijóo, R.A., 2021. Damage-driven strain localisation in networks of fibres: A computational homogenisation approach. *Comput. Struct.* 255, 106635.
- Roy, U., Zhou, M., 2020. A computational framework for predicting the fracture toughness of metals as function of microstructure. *J. Mech. Phys. Solids* 142, 103955.
- Simons, E., Weerheijm, J., Sluys, L.J., 2019. Simulating brittle and ductile response of alumina ceramics under dynamic loading. *Eng. Fract. Mech.* 216, 106481.
- Smyshlyaev, V.P., Cherednichenko, K., 2000. On rigorous derivation of strain gradient effects in the overall behaviour of periodic heterogeneous media. *J. Mech. Phys. Solids* 48 (6), 1325–1357.
- Toupin, R., 1962. Elastic materials with couple-stresses. *Arch. Ration. Mech. Anal.* 11, 385–414.
- Toupin, R., 1964. Theories of elasticity with couple-stress. *Arch. Ration. Mech. Anal.* 17, 85–112.
- Vasiliev, V., Lurie, S., Solyaev, Y., 2021. New approach to failure of pre-cracked brittle materials based on regularized solutions of strain gradient elasticity. *Eng. Fract. Mech.* 258, 108080.
- Vasoya, M., Lazarus, V., Ponson, L., 2016. Bridging micro to macroscale fracture properties in highly heterogeneous brittle solids: weak pinning versus fingering. *J. Mech. Phys. Solids* 95, 755–773.
- Wang, N., Xia, S., 2017. Cohesive fracture of elastically heterogeneous materials: An integrative modeling and experimental study. *J. Mech. Phys. Solids* 98, 87–105.
- Xiang, M., Jiang, S., Cui, J., Xu, Y., Chen, J., 2021. Coupling of dynamic ductile damage and melting in shock-induced micro-spalling: Modeling and applications. *Int. J. Plast.* 136, 102849.
- Yang, H., Abali, B.E., Müller, W.H., Barboura, S., Li, J., 2022. Verification of asymptotic homogenization method developed for periodic architected materials in strain gradient continuum. *Int. J. Solids Struct.* 238, 111386.
- Zinszner, J., Erzar, B., Forquin, P., Buzaud, E., 2015. Dynamic fragmentation of an alumina ceramic subjected to shockless spalling: an experimental and numerical study. *J. Mech. Phys. Solids* 85, 112–127.